Received: 27 July 2022 | Revised: 22 December 2022 | Accepted: 20 January 2023

DOI: 10.1111/gbb.12839

ORIGINAL ARTICLE

Genes, Brain and Behavior

Morphological and sensorimotor phenotypes in a zebrafish CHARGE syndrome model are domain-dependent

Dana R. Hodorovich[1] | Patrick M. Lindsley[1,2] | Austen A. Berry[1,3] | Derek F. Burton[1,4] | Kurt C. Marsden[1,4]

[1]Department of Biological Sciences, North Carolina State University, Raleigh, North Carolina, USA

[2]University of Virginia School of Medicine, University of Virginia, Charlottesville, VA, USA

[3]Biogen, Durham, NC, USA

[4]Washington University, St. Louis, MO, USA

Correspondence
Kurt C. Marsden, Department of Biological Sciences, North Carolina State University, Raleigh, NC, USA.
Email: kcmarsde@ncsu.edu

Funding information
CHARGE Syndrome Foundation, Grant/Award Number: Pilot grant; National Institute of Neurological Disorders and Stroke, Grant/Award Number: R21NS120079-01

Abstract

CHARGE syndrome is a heterogeneous disorder characterized by a spectrum of defects affecting multiple tissues and behavioral difficulties such as autism, attention-deficit/hyperactivity disorder, obsessive–compulsive disorder, anxiety, and sensory deficits. Most CHARGE cases arise from *de novo*, loss-of-function mutations in chromodomain-helicase-DNA-binding-protein-7 (CHD7). CHD7 is required for processes such as neuronal differentiation and neural crest cell migration, but how CHD7 affects neural circuit function to regulate behavior is unclear. To investigate the pathophysiology of behavioral symptoms in CHARGE, we established a mutant *chd7* zebrafish line that recapitulates multiple CHARGE phenotypes including ear, cardiac, and craniofacial defects. Using a panel of behavioral assays, we found that *chd7* mutants have specific auditory and visual behavior deficits that are independent of defects in sensory structures. Mauthner cell-dependent short-latency acoustic startle responses are normal in *chd7* mutants, while Mauthner-independent long-latency responses are reduced. Responses to sudden decreases in light are also reduced in mutants, while responses to sudden increases in light are normal, suggesting that the retinal OFF pathway may be affected. Furthermore, by analyzing multiple *chd7* alleles we observed that the penetrance of morphological and behavioral phenotypes is influenced by genetic background but that it also depends on the mutation location, with a chromodomain mutation causing the highest penetrance. This pattern is consistent with analysis of a CHARGE patient dataset in which symptom penetrance was highest in subjects with mutations in the CHD7 chromodomains. These results provide new insight into the heterogeneity of CHARGE and will inform future work to define CHD7-dependent neurobehavioral mechanisms.

KEYWORDS
behavior, CHARGE syndrome, chd7, CRISPR/Cas9, zebrafish

1 | INTRODUCTION

CHARGE syndrome is an autosomal dominant disorder that affects approximately 1 in every 10,000 births.[1] CHARGE is an acronym describing the previously used diagnostic criteria, but disease diagnosis now includes the presentation of at least one major feature including coloboma of the eye, atresia of the choanae, and semicircular canals defects, or a major sign with additional minor symptoms

including heart or esophageal anomalies[2] cleft lip/palate, cranial nerve(s) dysfunction,[3] and developmental delay.[4] In addition to these symptoms, ~60% of CHARGE patients are prescribed medication for mood and/or behavioral difficulties.[5] These include hypo- or hypersensory processing problems,[6] autistic-like behaviors,[7] obsessive–compulsive disorder and repetitive behaviors,[8] attention-deficit/hyperactivity disorder (AD/HD),[9] anxiety,[6] aggression,[5] diminished self-regulation,[6] self-abusive behaviors,[5,10] sleep issues[9] and intellectual disability.[11] Despite their frequency, the pathophysiology of behavioral symptoms in CHARGE patients is not well understood.

De novo loss-of-function mutations in the chromatin remodeling gene *Chromodomain-helicase-DNA-binding-protein 7* (CHD7) cause ~70% of CHARGE cases.[12,13] Mutations have been found throughout the gene and include a variety of missense, nonsense, frameshift, and splice site mutations,[14–16] indicating there is no hotspot for disease pathogenesis. CHD7 is an ATP-dependent transcriptional regulator ubiquitously expressed with enhanced expression in the developing brain.[17] CHD7 has multiple roles in neurodevelopment including neural crest cell migration and differentiation,[18,19] cerebellar organization and foliation,[20,21] olfactory development,[22,23] regulation of myelination and remyelination factors,[24] and glial and neuronal differentiation.[25] Animal models of CHARGE syndrome have provided insight into the etiology of ear and vestibulocochlear defects,[26] gonadal deficits, interventricular heart deficits,[22,26] gut motility dysfunction,[27] and craniofacial defects.[28–30] Here we sought to build on these efforts, using CRISPR/Cas9 to generate a new zebrafish CHARGE model and define how CHD7 regulates sensorimotor behavior.

Our model recapitulates several CHARGE phenotypes including ear, heart, and craniofacial defects, and our data also show that *chd7* is required for specific visual and auditory behaviors. Loss of *chd7* alters behavioral selection following acoustic stimulation, a phenotype that is both context-dependent and independent of defects in sensory structures. Finally, by analyzing multiple zebrafish CHARGE models, we find that the location of the mutation within the *chd7* gene affects the penetrance of CHARGE-related morphological and behavioral deficits. Our data support the highly conserved functions of CHD7 and reflect the heterogeneity of CHARGE syndrome patients. Together, our data provide new insight into the causes of variation in CHARGE presentation.

2 | MATERIALS AND METHODS

2.1 | *Danio rerio* husbandry and maintenance

All animal use and procedures were approved by the North Carolina State University Institutional Animal Care and Use Committee. *chd7* crispants and Exon 9, 2nd chromodomain line (*chd7*$^{ncu101/+}$) were maintained in the *Tüpfel long fin* (TLF) background. The TLF strain originated from University of Pennsylvania stocks. The Exon 16, ATP-helicase domain line (*chd7*$^{rdu1002/+}$), gifted by Dr. Erica Davis from Northwestern University, was maintained in the AB and TLF background. Adult zebrafish were housed in 5 fish/L density under a 14 h:10 h light:dark cycle at ~28°C, and were fed rotifers, *artemia* brine shrimp (Brine Shrimp Direct), and GEMMA micro 300 (Skretting).

To generate embryos for larval testing, male and female pairs were placed in mating boxes (Aquaneering) containing system water and artificial grass. 1–2 h into the subsequent light cycle of the following day, embryos were collected and placed into petri dishes containing 1× E3 embryo media. Embryos were sorted for fertilization under a dissecting scope at ~6 h post fertilization (hpf) and placed into 10 cm petri dishes with $n \leq 65$. All embryos were reared in a temperature-controlled incubator at 29°C on a 14 h:10 h light:dark cycle. Each day until testing, a 50%–75% media change was performed. All experiments were performed blind to genotype.

2.2 | Generation of *chd7*$^{ncu101/+}$ and *chd7* crispants

Single guide RNAs (Table S4) were designed using CHOPCHOP (https://chopchop.cbu.uib.no/) and CRISPRscan (https://www.crisprscan.org/) using the zebrafish reference genome (GRCz11). Selected crRNAs contained a minimum of four nucleotide mismatches at off-target sites in the zebrafish genome and were verified by Integrated DNA Technologies (IDT) CRISPR-Cas9 guide RNA design checker and NCBI Nucleotide Basic Local Alignment Tool. Target-specific crRNAs, mismatched crRNA, universal scaffold tracrRNAs, and Alt-R® S.p. HiFi Cas9 Nuclease V3 and gRNA duplexes were purchased from (IDT). gRNA duplexes and Cas9-gRNA ribonucleoproteins were generated according to the manufacturer's protocol. Microinjections into one-cell stage embryos were performed with a 50 µM injection mix containing the gRNA duplex, IDT Alt-R® S.p. HiFi Cas9 Nuclease V3 [15.5 µM], 0.5% phenol red, and nuclease-free H_2O. Embryos were generated by crossing TLF wild-type pairs. *chd7* mutagenesis was confirmed in injected larvae using the IDT genomic cleavage assay detection kit with T7 endonuclease digestion and/or by Sanger sequencing.

2.3 | DNA extraction and genotyping via PCR

Larvae were individually placed in 96-well plates containing methanol (MeOH) for tissue fixation. DNA was extracted from whole larvae using a lysis buffer of 25 mM sodium hydroxide, 0.2 mM EDTA (base solution), and 40 mM Tris–HCl (neutralization solution). For the Exon 9, 7 bp deletion mutation (*chd7*$^{ncu101/}$) forward and reverse primers amplified a 289 bp fragment (wild-type). Amplicons were resolved on a 3% agarose gel using gel electrophoresis. For the Exon 16, 1 bp deletion mutation (*chd7*$^{rdu1002/}$) forward and reverse primers amplified a 349 bp fragment (wild-type). The 1 bp deletion created a unique restriction site; amplicons were digested with *XcmI* and the 349 bp wild-type and 254 bp mutant bands were resolved on a 1% agarose gel (Table S5).

2.4 | Morphology and survival assessments

2.4.1 | Morphological phenotypes and brightfield imaging

Larvae were assessed for morphological phenotypes at 5–6 days post-fertilization (dpf) and imaged using brightfield microscopy (Nikon SMZ25). Larvae were anesthetized in 0.2% Tricaine (MS-222) in 1× E3 and laterally mounted in 1.5% low-melting point agarose in 1× E3 medium. Images were acquired at 10× total magnification, and phenotypes were scored following image capture. Larvae were unmounted and individually placed in 96-well plates containing MeOH for tissue fixation, DNA extraction, and genotyping. Images were masked from genotype during assessment, and manually scored by two independent experimenters. Craniofacial defects were determined by the presence of a lower jaw protrusion, and/or flattened or extremely sloped head from the most dorsal part of the head to the most anterior part of the upper jaw, adjacent to the eye. Examples of craniofacial phenotypes were referenced from previously published studies in larval zebrafish and CHARGE syndrome.[28–30]

2.4.2 | Lateral line/neuromast staining and imaging

Lateral line neuromasts were assessed using DASPEI (2-[4-(Dimethylamino)styryl]-N-ethylpyridinium iodide) (Fisher Scientific) stain. Larvae were submerged in 1× E3 medium containing 0.007% DASPEI for 15 min at room temperature. Larvae were quickly washed with fresh 1× E3 medium three times and anesthetized with 0.2% Tricaine. Larvae were laterally mounted in 1.5% low-melting point agarose in 1× E3 medium and imaged with a fluorescent dissecting scope at 10× total magnification (Nikon SMZ25). The total number of neuromasts were counted manually while blind to genotype. Randomly selected larvae were then imaged at high-resolution using a 3i Mariana Spinning Disk Confocal (Hamamatsu ImagEM X2 back-thinned EM CCD camera) at 63× total magnification. *Z*-stacks were acquired with a 488 nm solid state laser and at a step size of 0.5 μm ($n = 2$ neuromasts per fish). Confocal imaging of the neuromasts were performed on the same two neuromasts located directly caudal to the swim bladder. Larvae were unmounted and placed in 96-well plates containing MeOH for tissue fixation, DNA extraction, and genotyping. All images were processed with ImageJ/Fiji.

2.5 | Survival analysis

For survival assessments, larvae were tracked daily from ~6 hpf until 30 dpf. By 6 dpf larvae were reared in system water, co-cultured with rotifers, and received fresh rotifers on 9, 12, 15 dpf in addition to daily GEMMA micro 75 (Skretting) feeding. By 17 dpf, juveniles were fed daily with GEMMA micro 150 and 300 (Skretting) and *artemia* brine shrimp (Brine Shrimp Direct). Fish were inspected at the same time each day, and dead fish were removed and individually placed in MeOH for future genotyping. At 30 days, the remaining juveniles were euthanized and processed for genotyping.

2.6 | Behavioral analyses

Larvae were tested at 5–6 dpf within their normal light cycle. Larvae were screened for severe morphological defects affecting mobility including large pericardial edema and bent/missing tails. Swim bladder inflation and less severe defects (those not affecting mobility) were ignored. Post-screening, larvae adapted to the testing lighting and temperature conditions for 30 min before placement in a custom laser-cut acrylic grid consisting of 36 9 mm diameter wells. The grid is anchored to a 60 × 5 × 5 mm aluminum rod attached to an acoustic shaker (Bruel and Kjaer). Spontaneous movement, acoustic startle, short-term habituation, dark-flash, and light-flash assays were tracked and analyzed using FLOTE-software as previously described.[31–33] The long-term locomotor behavioral assay was performed using the DanioVision (Noldus) apparatus and analyzed using EthoVision XT video tracking (Noldus).

2.7 | Spontaneous movement

Once placed into the 36-well grid, larvae acclimated for 3 min and were then recorded for 18.5 min at 50 fps at 640 × 640 px resolution.

2.8 | Acoustic startle response and auditory behaviors

Larvae acclimated for 2 min prior to auditory stimulus onset. Larvae received a total of 60 acoustic stimuli: 10 pseudorandomized trials of 6 intensities (13.6, 25.7, 29.2, 35.5, 39.6, and 53.6 dB), with a 20 s inter-stimulus interval (ISI). Immediately following the acoustic startle response assay, larvae received 30 additional acoustic stimuli (53.6 dB) with a 1 s ISI to induce short-term habituation. Recordings were captured at 1000 fps and 640 × 640 px resolution.

2.9 | Visual startle responses, dark-flash/light-flash

Larvae acclimated in dim white light via an LED light (0.4 V) for 3 min prior to dark-flash onset. Larvae received a total of 10 "dark-flashes" or 1 s intervals of the light turning off with a 30 s ISI. Next, larvae received a total of 10 "light-flashes" or 1 s intervals of bright light (10 V). Recordings were captured at 1000 fps and 640 × 640 px resolution.

2.10 | RNA extraction and cDNA synthesis

For qPCR analysis, 5 dpf larvae were anesthetized using 0.2% Tricaine in 1× E3 medium. Larval heads were dissected using a 15°, 5 mm scalpel, briefly washed in 1× PBS, and placed in a 96-well plate containing ~200 μL *RNALater* (Invitrogen). Remaining tissue was placed in a corresponding well containing MeOH for DNA extraction and

genotyping. Heads were briefly chilled on ice and placed in 4°C overnight for *RNAlater* permeation. Following ~8 h incubation, heads were moved to −20°C. Once genotypes were obtained, wild-type, heterozygous, and mutant heads were pooled for RNA extraction (3 biological replicates per genotype). Tissue was homogenized using Trizol, and RNA was extracted using RNeasy Mini kits (Qiagen, ID: 217084) according to manufacture protocol. For cDNA synthesis, 1 ng–5 μg of RNA per reaction was used in SuperScript™ First-Strand synthesis kits (Invitrogen, ID: 11904018). Nucleic acid purity was assessed using a NanoPhotometer® (Implen).

2.11 | qPCR

qPCR was performed with SYBR® Green PCR master mix. For *chd7*, forward and reverse intron-spanning primers annealed downstream of the mutation targets in the 2nd chromodomain (*chd7*$^{ncu101/}$) and ATP-helicase domain (*chd7*$^{rdu1002/}$) alleles. Primers specific to e*if1a* were used for quality control and normalizing *chd7* expression data (Table S5).

2.12 | Statistics

Statistical analyses were completed using Prism 8 (GraphPad). All datasets were tested for normality using the Shapiro–Wilk test. ANOVA and multiple comparisons, or Kruskal Wallis, nonparametric tests and Dunn's multiple comparisons were used, respectively. For all experiments and data sets, the *p*-value threshold was set to $\alpha = 0.05$. All data are represented as mean ± standard deviation, unless otherwise noted in the figure legends.

3 | RESULTS

3.1 | CRISPR/Cas9-generated *chd7* mutants recapitulate CHARGE phenotypes

Zebrafish larvae are an excellent animal model for examining the mechanisms underlying developmental and behavioral deficits in CHARGE syndrome because of their shared genetics, including 82% of disease-related genes,[34] accessibility to genetic manipulation, conserved vertebrate structures within the central nervous system, along with their small size and extensive behavioral repertoire that allows for high-throughput testing.[35,36] Zebrafish Chd7 shares ~68% amino acid identity with human CHD7 including high conservation within each functional domain (Chromodomains = 71.22%; ATP-Helicase domain = 92.7%; SANT domain = 78.33%; BRK domains = 75%). Larval zebrafish CHARGE syndrome models have previously been generated through morpholino knock-down of *chd7* and more recently using CRISPR/Cas9, and they have been used to investigate specific phenotypes such as craniofacial,[28] heart,[37] and gut defects.[27] To generate a stable *chd7* mutant line for investigating disease-related phenotypes and a panel of sensorimotor behaviors, we designed a single guide RNA (gRNA) targeting a highly conserved region in Exon 9 that contributes to the second chromodomain. We microinjected this gRNA along with Cas9 protein into 1-cell stage TLF-strain zebrafish embryos. We raised injected embryos to adulthood, crossed them to wild-type TLF fish, and PCR-amplified and sequenced the gRNA target site in F_1 offspring to assess germ-line transmission of CRISPR/Cas9-induced mutations. We identified a 7-base pair (bp) deletion that produces a frameshift and premature stop codon within the second chromodomain of Chd7 (*chd7*$^{ncu101/}$) (Figure 1A). First, we assessed the viability of chromodomain mutants until 30 days post fertilization (dpf) and found that by 15 dpf in contrast to the 90% survival rate of wild-types, only 24% of chromodomain mutants and 59% of heterozygotes survived (Figure 1B), with no changes in viability thereafter. These data are similar to those showing embryonic lethality of homozygous *chd7* mutations in mammals,[26] but the semi-viability of our zebrafish *chd7* mutants establishes an opportunity to evaluate *chd7* function in a homozygous context. We next used RT-qPCR to measure *chd7* transcript levels in pools of 5 dpf larvae and observed that *chd7* mRNA was significantly downregulated by 22% in chromodomain heterozygotes and by 54% in mutants, verifying the deleterious impact of the mutation, with the residual transcript likely reflecting *chd7* maternal deposition[28] and/or incomplete nonsense-mediated decay (Figure 1C).

To determine whether our larval zebrafish model recapitulates CHARGE-related developmental phenotypes, we examined the morphology of 5 dpf *chd7* larvae. Both chromodomain mutants and heterozygous siblings frequently displayed craniofacial defects, uninflated swim bladders, enlarged pericardial area, and ear defects (Figure 1E). We did not observe differences in body length or eye size. In teleost fish, the otoliths, hard crystal-like structures within the otic vesicle, are tethered to the sensory hair cells and function in hearing and balance.[38,39] We observed a variety of otolith phenotypes in chromodomain mutants and heterozygotes, including small anterior otoliths, missing anterior or posterior otoliths, and a merged or misshapen phenotype (Figure 1F). These defects occurred both unilaterally and bilaterally. Otolith defects were the most penetrant phenotype, with 26% of heterozygotes and 59% of mutants displaying a phenotype. This reflects the case with human CHARGE patients, as inner and outer ear defects are the most common phenotype with at least 80% of patients reporting ear anomalies across clinical studies.[4] Overall, 29% of chromodomain heterozygotes and 75% of mutants displayed at least one morphological phenotype (Table 1).

To verify the impact of germline mutations in *chd7* on these developmental phenotypes, we analyzed an independent *chd7* mutant line that was generated in the AB wild-type strain using CRISPR/Cas9 with a gRNA targeting Exon 16 (Figure 1A; gifted by Dr. Erica Davis, Northwestern University). The identified 1 bp deletion creates a premature stop codon within the ATP-helicase domain (*chd7*$^{rdu1002/}$), and using RT-qPCR we found that *chd7* transcript levels in ATP-helicase domain mutants were significantly downregulated (Figure 1D), as in chromodomain mutants. We observed similar morphological phenotypes in ATP-helicase domain mutants, but with decreased

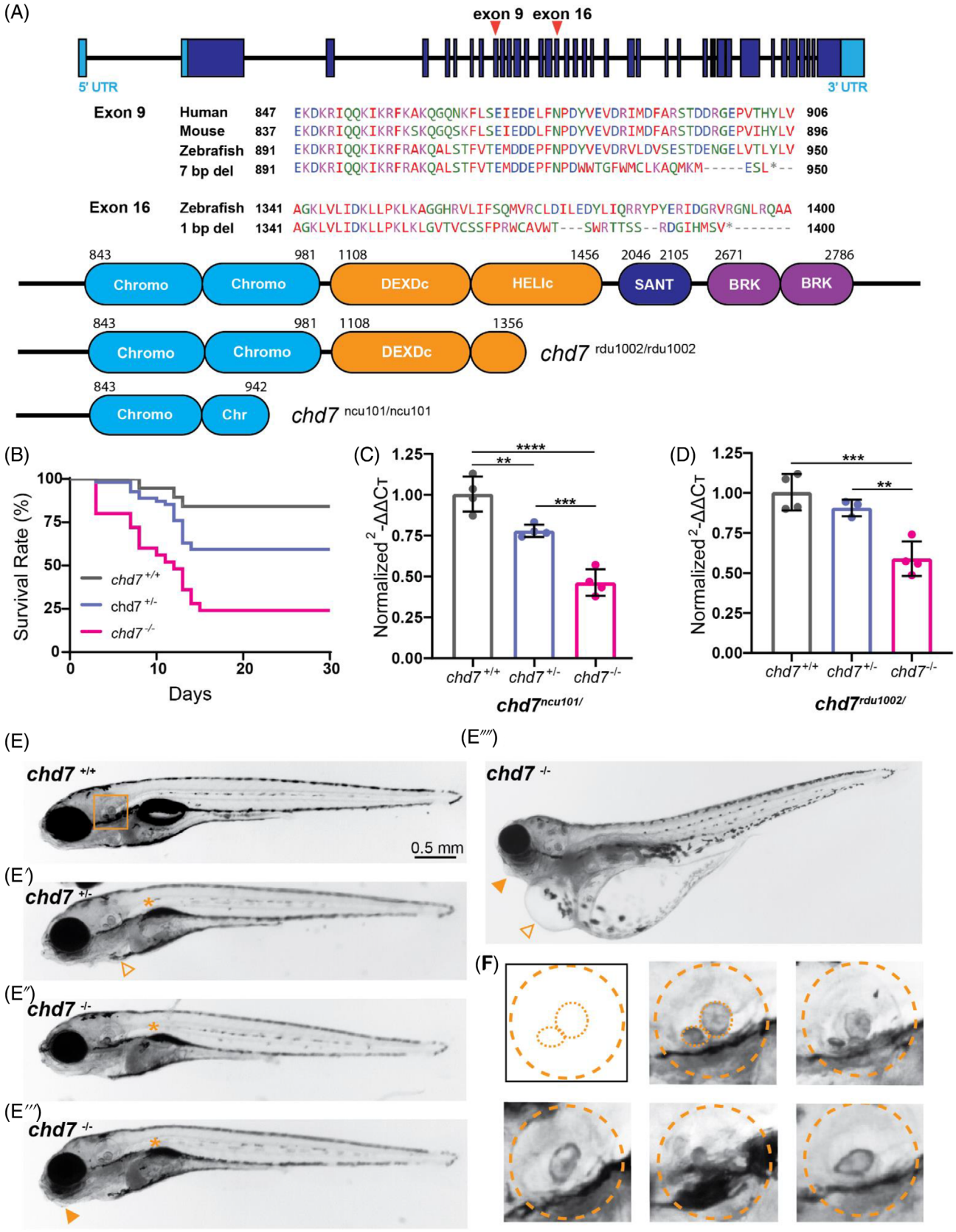

FIGURE 1 Legend on next page.

penetrance in heterozygotes. In contrast to chromodomain larvae, there was a striking absence of otolith defects in both ATP-helicase domain heterozygous and mutant larvae (Table 1). To test one possible explanation for this difference in otolith phenotypes and for the presence of phenotypes in a small number of chromodomain wild-type siblings, we investigated whether there were CRISPR-induced

TABLE 1 Morphological phenotype frequencies in chromodomain and ATP-helicase domain mutants. Morphological phenotype ratio and frequencies in 5–6 dpf *chd7*$^{+/+}$ siblings, *chd7*$^{ncu101/+}$, *chd7*$^{ncu101/ncu101}$, *chd7*$^{rdu1002/+}$, and *chd7*$^{rdu1002/rdu1002}$. Chromodomain larvae are in TLF zebrafish strain, and ATP-helicase domain larvae are in AB zebrafish strain.

		Craniofacial defect	Otolith defect	Pericardial edema	Noninflated swim bladder	Larvae with any morphological phenotype
Chromodomain larvae	*chd7*$^{+/+}$	1/25, 4%	3/25, 12%	2/25, 8%	-	4/25, 16%
	chd7$^{ncu101/+}$	2/68, 2.9%%	18/68, 26.4%	3/68, 4.4%	4/68, 5.9%	20/68, 29.4%
	chd7$^{ncu101/ncu101}$	4/37, 10.8%	22/37, 59.5%	8/37, 21.6%	15/37, 40.5%	28/37, 75.7%
ATP-helicase domain larvae	*chd7*$^{+/+}$	-	-	-	-	0/23
	chd7$^{rdu1002/+}$	1/42, 2.4%	-	2/42, 4.8%	3/42, 7.1%	5/42, 11.9%
	chd7$^{rdu1002/rdu1002}$	6/19, 31.6%	-	11/19, 57.9%	9/19, 47.4%	15/19, 78.9%

off-target mutations of the Exon 9 gRNA. We sequenced DNA from F_1 and F_2 chromodomain heterozygous adults for the top three predicted off-target locations (via chopchop.cbu.uib.no). There were no alterations to the base sequence of these potential off-target sites (Figure S1A), suggesting that rather than off-target effects of the gRNA the TLF strain used to generate the chromodomain mutant line may harbor genetic modifiers that influence the expression of morphological phenotypes. Having one or two copies of the chromodomain mutation greatly increases the penetrance of morphological phenotypes, however, all of which have previously been seen in *chd7* morphants.[28,30,37,40] Since both the chromodomain and ATP-helicase domain mutants survive through larval stages, have decreased *chd7* transcript, and recapitulate multiple but incompletely overlapping sets of disease-related phenotypes, these mutant lines provide a useful set of tools to study how different *chd7* mutations impact development and behavior.

3.2 | *chd7* is required for the central processing of auditory stimuli in the LLC circuit

Clinical studies have reported that at least 80% of CHARGE patients present with an external ear defect and either conductive or sensorineural hearing loss.[4] To determine if auditory detection was intact in our zebrafish CHARGE model, we performed an acoustic startle assay in 5 dpf larvae generated by crossing chromodomain heterozygous adults. Larvae received 60 acoustic stimuli, 10 trials at each of 6 intensities, with a 20 s interstimulus interval (ISI). Following an acoustic stimulus, zebrafish larvae perform one of two response types: (1) Short-latency C-bends (SLCs), which are initiated 4–15 ms after the stimulus and are driven by a pair of command-like reticulospinal neurons known as the Mauthner cells,[31] and (2) Long-latency C-bends (LLCs), which are initiated at least 15 ms after the stimulus, have reduced angular velocity, are independent of the Mauthner cells, and are mediated by a cluster of prepontine neurons in rhombomere 1.[31,41] Larval zebrafish bias their responses toward SLCs following strong acoustic stimuli and toward LLCs following weaker stimuli.[31] We did not observe any differences in SLC response frequency in either chromodomain heterozygotes or mutants (Figure 2A,B), indicating that auditory detection is largely intact. LLC responses, however, were significantly reduced in chromodomain mutants (Figure 2C,D), suggesting that there is a specific defect within the LLC circuit.

Following repeated strong acoustic stimulation, larval zebrafish display a simple form of non-associative learning, short-term habituation, in which SLC response frequency rapidly decreases.[42,43] As SLCs decrease, larvae briefly shift their response bias to perform more LLCs, and eventually ignore the stimulus altogether.[44] We tested whether *chd7* is required for this behavioral plasticity by presenting larvae with 30 acoustic stimuli at 53.6 dB with a 1 s ISI. When we analyzed the half-life of SLC frequency curves during habituation, we

FIGURE 1 CRISPR/Cas9 generated chd7 mutants recapitulate CHARGE syndrome related phenotypes. (A) Exon-intron structure of zebrafish *chd7* with CRISPR exon 9 and exon 16 targeted regions noted; amino acid alignment and conservation of Exon 9, 2nd chromodomain target across species, identified 7 bp deletion from mutagenesis; amino acid alignment of Exon 16, ATP-helicase domain target, and identified 1 bp deletion from mutagenesis; predicted Chd7 protein domains in wild-type (top), ATP-helicase domain 1 bp deletion allele (*chd7*$^{rdu1002/rdu1002}$), and chromodomain 7 bp deletion allele (*chd7*$^{ncu101/ncu101}$), additional target regions from sgRNAs noted. (B) Survival rate (%) of *chd7*$^{+/+}$ ($n = 19$), *chd7*$^{ncu101/+}$ ($n = 54$), and *chd7*$^{ncu101/ncu101}$ ($n = 25$) siblings during a 30-day period. (C) qPCR analysis of *chd7* mRNA in 5 dpf larvae (*chd7* $^{ncu101/}$, chromodomain allele), normalized to wild-type siblings. Each point represents a biological replicate of pooled larvae (per pool, *chd7*$^{+/+}$ $n \sim 12$–13; *chd7*$^{ncu101/+}$ $n \sim 20$–21; *chd7*$^{ncu101/ncu101}$ $n \sim 13$–14). (D) qPCR analysis of *chd7* mRNA in 5 dpf larvae (*chd7*$^{rdu1002/}$, ATP-helicase domain allele), normalized to wild-type siblings. Each point represents a biological replicate of pooled larvae (per pool, *chd7*$^{+/+}$ $n \sim 13$–14; *chd7*$^{rdu1002/-}$ $n \sim 22$–23; *chd7*$^{rdu1002/rdu1002}$ $n \sim 11$–12) (mean ± SD, Ordinary one-way ANOVA with Tukey's multiple comparisons, *$p < 0.05$, **$p < 0.01$, ***$p < 0.001$,****$p < 0.0001$). (E) Bright-field images of 5 dpf larvae (*chd7*$^{+/+}$, *chd7*$^{ncu101/+}$, *chd7*$^{ncu101/ncu101}$) with examples of morphological phenotypes including uninflated swim bladder (asterisk), pericardial edema (triangle), and craniofacial defects (solid triangle). (F) Examples of varying otolith defects in *chd7*$^{ncu101/}$, dashed orange lines represent morphology of the otic vesicle, and anterior and posterior otoliths.

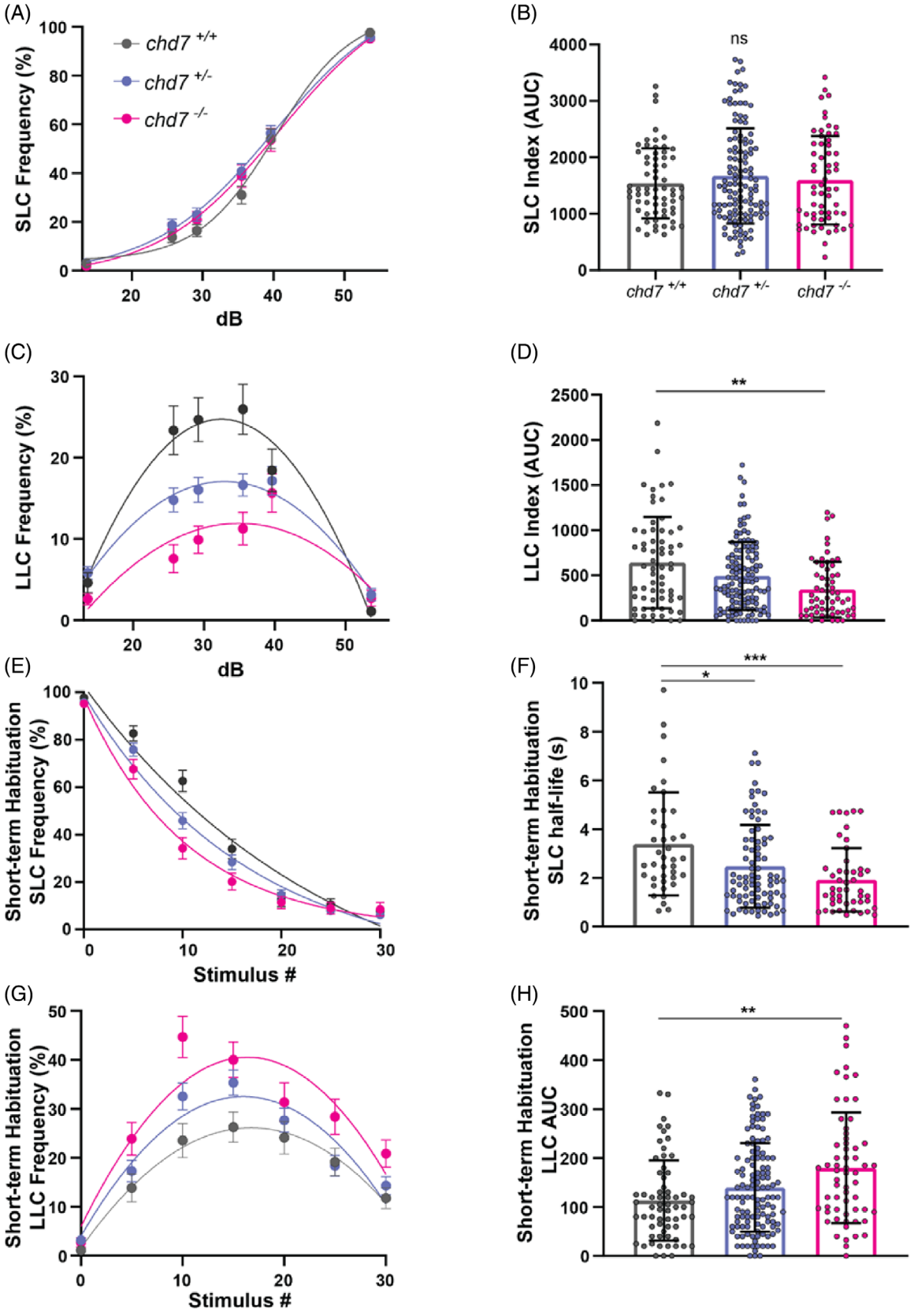

FIGURE 2 Legend on next page.

found that chromodomain mutants and heterozygotes habituate significantly faster than their wild-type siblings (Figure 2E,F). Like their siblings, mutants shift their response bias toward LLCs, but this shift is exaggerated as they perform significantly more LLCs (Figure 2G,H). These data indicate that the LLC response deficit we observed earlier following weaker, non-habituating stimuli (Figure 2C,D) is context-

dependent. Furthermore, these results suggest that *chd7* function is required to properly modulate activity in both the SLC and LLC circuits.

Having identified a defect in auditory behavior in *chd7* mutants, we next sought to determine whether this could be explained by the otolith malformations we observed (Figure 1E,F, Table 1). Thus, we assessed auditory responsiveness in an independent cohort of larvae using the same 60-stimulus assay, after which all larvae were then examined bilaterally for otolith defects and then genotyped. As before, SLC responsiveness was normal in all groups (Figure 3A,B), and we found that LLC responses were decreased in chromodomain mutants and heterozygotes regardless of otolith defects (Figure 3C,D). To account for another possible sensory contribution to the auditory deficits, lateral line neuromasts were examined using the vital dye, DASPEI, in a separate cohort of larvae. The lateral line has defined connections to the Mauthner cell SLC circuit.[45,46] Total neuromast number and morphology of individual hair cell clusters were not significantly different in chromodomain mutants and heterozygotes compared with wild-type siblings (Figure S2). Thus, the LLC deficit is independent of ear morphology and the lateral line, and thus it likely arises from a defect in the central processing of auditory stimuli. To determine if motor function downstream of the SLC and LLC initiation circuits is disrupted by *chd7* loss of function, we analyzed the kinematic performance of both response types. For SLCs, latency, turn angle, and duration were normal in mutants, while the distance traveled during SLC responses was slightly reduced in mutants (Figure S3A–D). For LLCs, all kinematic parameters were normal (Figure S3E–H). These data indicate that motor function is largely normal in *chd7* mutants.

We next tested the ATP-helicase domain mutant line using the same acoustic startle assay to confirm the role of *chd7* in these auditory behaviors. As with the chromodomain mutants, SLC response frequency was normal in ATP-helicase domain heterozygotes and mutants (Figure S4A,B). LLC response frequency, however, was not statistically significantly affected in ATP-helicase domain mutants, although there was a downward trend (Figure S4C,D). We also observed similar trends for short-term habituation, during which mutants' SLCs habituated faster (Figure S4E,F), while LLCs were increased (Figure S4G,H). ATP-helicase domain mutants also displayed minor SLC kinematic defects, including increased latency, decreased turn angle, and reduced distance traveled (Figure S5). It is possible that differences in the wild-type strain used to generate the two mutant lines may account for the phenotypic differences we observed between the two alleles. To test for this possibility, we propagated the ATP-helicase domain allele into the TLF strain for one generation and again tested auditory behavior in their offspring. Although less pronounced than the LLC deficit in chromodomain mutants, we measured a significant reduction in LLC frequency in these ATP-helicase domain mutants (Figure S6D). These data suggest that strain can influence the expression of auditory behavior phenotypes in *chd7* mutants.

To further clarify the contribution of *chd7* mutations to auditory responsiveness, we performed a complementation test by crossing chromodomain ($chd7^{ncu101/+}$) and ATP-helicase domain heterozygotes ($chd7^{rdu1002/+}$). To account for strain, the adult ATP-helicase domain heterozygotes used for all complementation crosses were from the TLF-derived generation. $chd7^{ncu101//rdu1002}$ double heterozygotes had intact SLC responses (Figure S6E,F), and there was a downward trend in their LLC response frequency compared with wild-type siblings (Figure S6G,H). That both chromodomain and ATP-helicase domain mutants show significantly reduced LLC responses when the genetic background is at least 50% TLF while $chd7^{ncu101//rdu1002}$ double heterozygotes only showed a trend indicates that there could be differential functional capacity of the two *chd7* alleles and/or that modifiers in the genetic background may influence the expression of the defect.

3.3 | *chd7* alleles produce varying visual and general locomotor phenotypes

Visual deficits are common in CHARGE patients,[47,48] and therefore we assessed visual responsiveness of chromodomain *chd7* mutants with multiple assays. First, we presented 5 dpf larvae with a series of "dark flashes" (sudden decreases in illumination) and "light flashes" (sudden increases in illumination), both of which elicit stereotyped, large-angle turns.[32] Chromodomain mutants performed significantly fewer dark-flash responses (Figure 4A), but their light flash responses were unaffected (Figure 4B). This could indicate that in zebrafish, *chd7* specifically regulates the OFF retinal pathway. We also tested ATP-helicase domain mutants for both dark-flash and light-flash responsiveness and found that neither behavior was significantly affected (Figure S7A,B). This phenotypic difference between the two

FIGURE 2 Loss of chd7 induces a context-dependent LLC phenotype in auditory driven behaviors. (A) Acoustic startle responses, average short-latency c-bend (SLC) frequency as acoustic stimulus intensity increases ($chd7^{+/+}$ $n = 64$, $chd7^{ncu101/+}$ $n = 127$, $chd7^{ncu101/ncu101}$ $n = 61$) (mean ± SEM). (B) Short-latency c-bend sensitivity index, calculated by the area under the SLC frequency curves for individual larvae (mean ± SD, Ordinary one-way ANOVA with Tukey's multiple comparison). (C) Long-latency c-bend (LLC) frequency as acoustic stimulus intensity increases (mean ± SEM). (D) Long-latency c-bend sensitivity index calculated by the area under the LLC frequency curves for individual larvae (mean ± SD, Kruskal-Wallis with Dunn's multiple comparisons). (E) Short-term habituation, average SLC frequency during 30 acoustic stimuli at highest intensity ($chd7^{+/+}$ $n = 40$, $chd7^{ncu101/+}$ $n = 82$, $chd7^{ncu101/ncu101}$ $n = 47$) (mean ± SEM). (F) SLC half-life calculated by nonlinear regression (one-phase exponential decay) of SLC frequency curves for individual larvae (mean ± SD, Kruskal-Wallis with Dunn's multiple comparisons). (G) Average LLC frequency during 30 acoustic stimuli at highest intensity (mean ± SEM). (H) LLC sensitivity index calculated by the area under the LLC frequency curves for individual larvae (mean ± SD, Kruskal-Wallis with Dunn's multiple comparisons, $^{*}p < 0.05$, $^{**}p < 0.01$, $^{***}p < 0.001$,$^{****}p < 0.0001$).

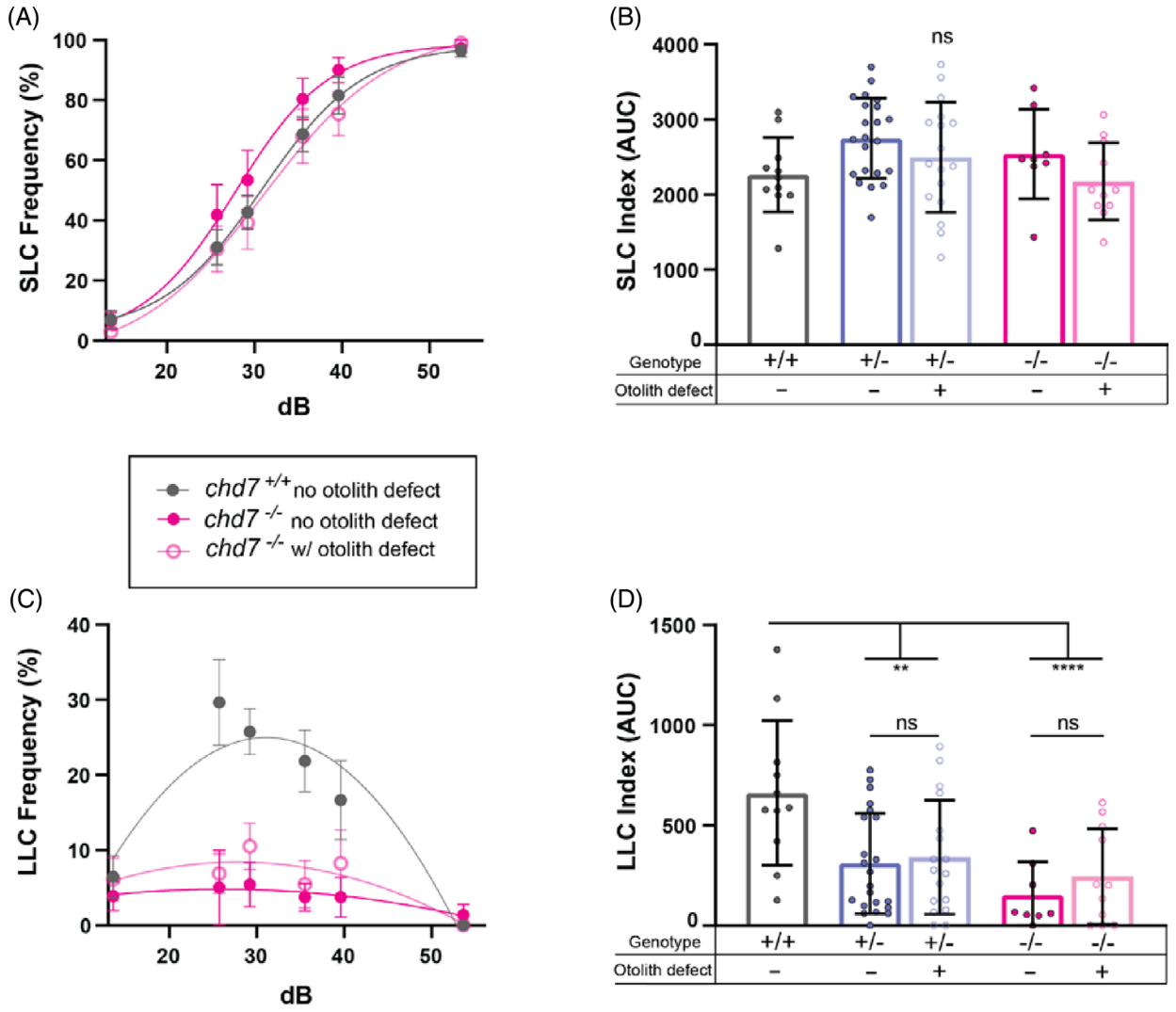

FIGURE 3 LLC deficit is independent of otolith morphology in *chd7* chromodomain mutants. (A) Acoustic startle responses, average short-latency c-bend (SLC) frequency comparing *chd7*$^{ncu101/+}$ and *chd7*$^{ncu101/ncu101}$ with or without otolith defects (*chd7*$^{+/+}$ $n = 11$, *chd7*$^{ncu101/+}$ w/o otolith defect $n = 22$, *chd7*$^{ncu101/+}$ with otolith defect $n = 17$, *chd7*$^{ncu101/ncu101}$ w/o otolith defect $n = 8$, *chd7*$^{ncu101/ncu101}$ with otolith defect $n = 11$) (mean ± SEM). (B) Short-latency c-bend sensitivity index, calculated by the area under the SLC frequency curves for individual larvae (mean ± SD, Ordinary one-way ANOVA with Tukey's multiple comparison). (C) Long-latency c-bend (LLC) frequency as acoustic stimulus intensity increases (mean ± SEM). (D) Long-latency c-bend sensitivity index calculated by the area under the LLC frequency curves for individual larvae (mean ± SD, Ordinary one-way ANOVA with Tukey's multiple comparison, $^{**}p < 0.01$, $^{****}p < 0.0001$).

alleles may reflect strain differences or that the location of the induced mutation within *chd7* influences phenotype penetrance. When we tested ATP-helicase domain mutants in the TLF background, we saw no phenotypes in either response, indicating that this visual phenotype is likely independent of strain (Figure S8A,B).

Having identified a defect in responses to visual stimuli, we aimed to determine if the defect extends to longer-term behavior patterns. We thus tested *chd7* mutants from both the chromodomain and ATP-helicase domain lines in an extended visuo-motor response (VMR) assay by dark-adapting 6 dpf larvae for 30 min, followed by 4 h of darkness and then 4 h in bright light conditions.[49] Chromodomain mutants showed no difference in movement during the dark phase, but in the light phase showed significant reduced activity (Figure 4C,D). ATP-helicase domain mutants showed a different pattern of activity, with mutants having normal activity in the light phase but hyperactivity in the dark phase (Figure 4E,F). This result replicates the dark-phase hyperactivity recently reported in an independent *chd7* mutant line in which CRISPR/Cas9 was used to target Exon 17,[49] which contributes to the same HELIc protein domain as Exon 16 (*chd7*$^{rdu1002/}$). We also analyzed larvae from a complementation cross of *chd7*$^{ncu1019/+}$ by *chd7*$^{rdu1002/+}$ adults and found no significant differences in distance traveled by double heterozygotes in both dark and light phases (Figure S9A,B). Strain likely does not account for these differences, as larvae for these experiments, including the

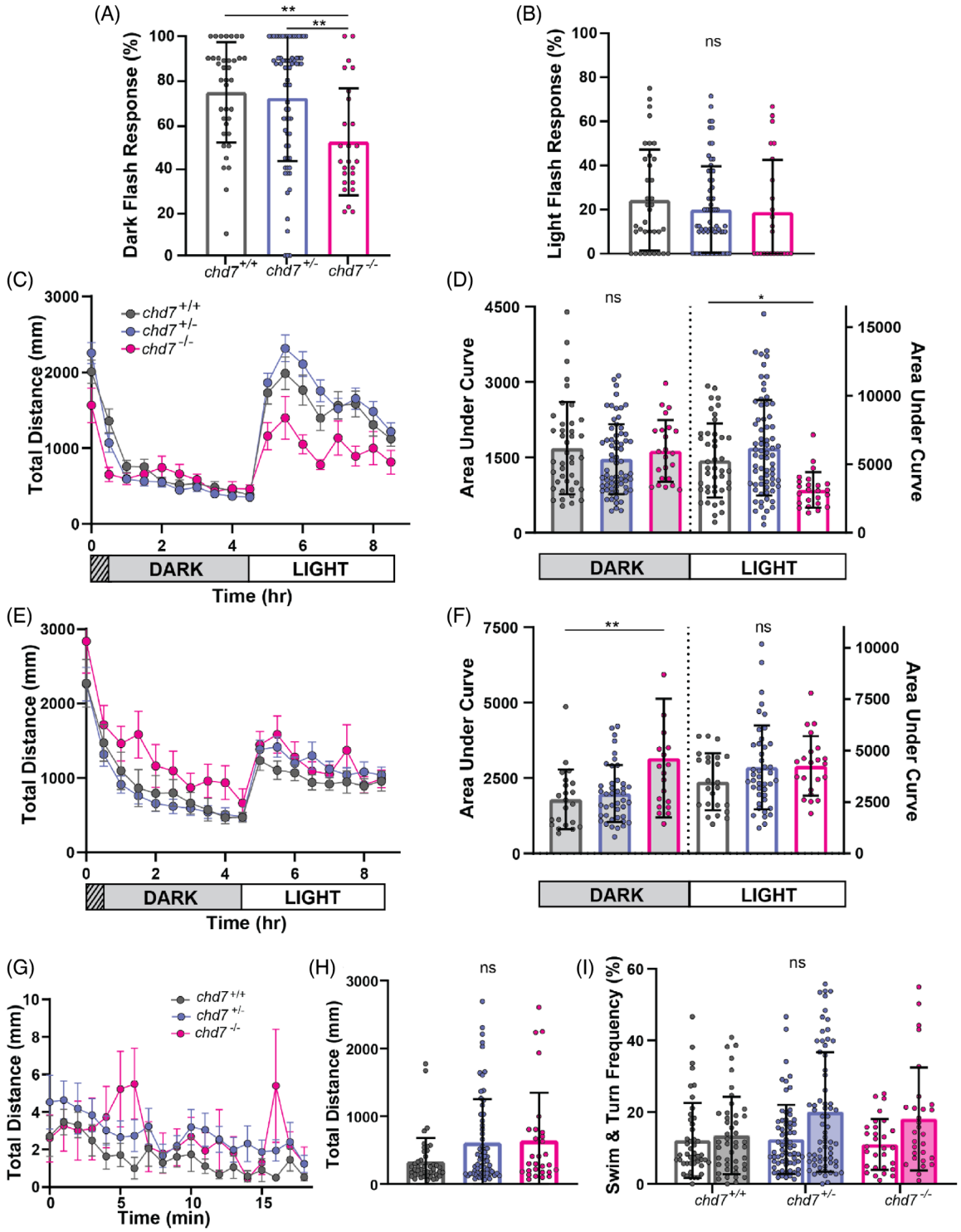

FIGURE 4 Hypo- and hyper-activity phenotypes in chromodomain and ATP-helicase domain mutants. (A) Chromodomain larval dark-flash and (B) light-flash response frequencies ($chd7^{+/+}$ $n = 37$, $chd7^{ncu101/+}$ $n = 69$, $chd7^{ncu101/ncu101}$ $n = 26$) (mean ± SD, Ordinary one-way ANOVA with Tukey's multiple comparison, $^{**}p < 0.01$). (C) Chromodomain larval average total distance traveled plot during 9 h of recording, analyzed every 30 min, including 1 h of acclimation in the dark, 4 h in the dark, and 4 h in light ($chd7^{+/+}$ $n = 44$, $chd7^{ncu101/+}$ $n = 70$, $chd7^{ncu101/ncu101}$ $n = 26$) (mean ± SEM). (D) Chromodomain larval area under the curve for individual distance plots during the dark or light phase (mean ± SD, Ordinary one-way ANOVA with Dunnett's multiple comparisons, $^{*}p < 0.05$). (E) ATP-helicase domain larval average total distance traveled ($chd7^{+/+}$ $n = 22$, $chd7^{rdu1002/+}$ $n = 42$, $chd7^{rdu1002/rdu1002}$ $n = 20$) (mean ± SEM) and (F) area under the curve during the dark or light phase (mean ± SEM (G) chromodomain larval total distance time plot during 18.5 min of recording ($chd7^{+/+}$ $n = 46$, $chd7^{ncu101/+}$ $n = 67$, $chd7^{ncu101/ncu101}$ $n = 29$) (mean ± SEM). (H) Sum of total distance traveled for individual larvae, (I) swim (open bars) and turn (shaded bars) frequencies (mean ± SD, Kruskal-Wallis with Dunn's multiple comparisons).

complementation cross, were all derived from the TLF strain. That both the chromodomain mutants' light-phase hypoactivity and the ATP-helicase domain mutants' dark-phase hyperactivity were complemented by the other allele provides further evidence that the two alleles have different functional capabilities.

Based on *chd7* mutants' altered activity levels (Figures S3 and S5), along with previous studies showing motor coordination defects, increased circling, and hyperactive behaviors in *Chd7* heterozygous mice,[21,26,50–52] we recorded spontaneous movements at 50 fps for 18.5 min to more closely observe potential motor deficits. Chromodomain mutants showed no difference in distance moved or in the frequency of swims or turns during the assay (Figure 4G,H,I). ATP-helicase domain mutants, however, displayed a significant increase in swim frequency, a hyperactive phenotype consistent with their dark-phase increase in locomotion (Figure S7E). Additionally, ATP-helicase domain mutants derived in the TLF background also displayed an increased swim frequency (Figure S8E), indicating a strain-independent phenotypic difference between the two alleles.

As the differences in behavioral phenotypes between the chromodomain and ATP-helicase domain *chd7* mutants cannot be entirely accounted for by the wild-type strain that was used, we next examined whether the differences in morphological phenotypes (Table 1) could be explained by strain differences. Comparing chromodomain mutants and ATP-helicase domain mutants, we found that ATP-helicase domain mutants did not display any otolith defects (Table 1), in stark contrast to the chromodomain mutants (Figure 1F, Table 1). ATP-helicase domain mutants had a higher frequency of craniofacial defects and pericardial edema. Overall, the frequencies of mutant larvae with any type of morphological defect were similar for both alleles, but the frequency of *chd7* heterozygous larvae with morphological defects was substantially higher in chromodomain mutants. We thus assessed morphological defects in larvae derived from a complementation cross of chromodomain and ATP-helicase domain heterozygotes (TLF derived), and we observed the presence of all previously observed defects (Table S1), indicating a clear failure to complement. Together, the differences in both behavioral and morphological defects between the chromodomain and ATP-helicase domain mutants suggest that the location of the mutation in the *chd7* gene impacts the expression of CHARGE-related phenotypes.

3.4 | CHARGE-related phenotypes depend on *chd7* mutation location

To directly test if morphological and behavioral phenotypes in *chd7* mutants are dependent on the location of the mutation, we injected 1-cell stage TLF-strain embryos with CRISPR/Cas9 ribonucleoproteins (RNPs) using unique gRNAs targeting a site early in the gene (Exon 3), the middle of the gene (Exon 9), late in the gene (Exon 30), or a mixture of all three. All guide target sites are present in the major transcripts of *chd7*. The targeted regions were in the low complexity domain 12, chromodomain 2, and low complexity domain 21, respectively. Embryos injected with Cas9 protein but without a gRNA served as vehicle controls. To control for possible non-specific effects of the Cas9-gRNA complex, we also designed a mismatched gRNA with no binding sites in the zebrafish genome. We observed no behavioral differences between uninjected, Cas9 injected, and mismatched gRNA plus Cas9 injected larvae (Figure S10). Frequency of genomic editing events was determined by sequencing individual crispants (Figure S11A,B,C). Exon 3 and 9 guides induced edits in 95% of crispants analyzed, while Exon 30 induced edits in 93% of crispants, indicating all three guides are highly efficient at inducing edits at their respective target site. At 5 dpf, larvae injected with just a single gRNA displayed lower frequencies of morphological phenotypes compared with the stable mutant lines (Table 2). Larvae injected with the 3-gRNA mixture showed similar phenotype frequencies to the stable lines, except for otolith defects, which were reduced compared with chromodomain mutants. Of the larvae injected with one gRNA, morphological phenotype frequencies were similar for Exon 9 and Exon 30 but were lowest for Exon 3. This result is contrary to a common CRISPR strategy of targeting a site early in the gene to produce the strongest effects. Given the similar rates of editing for all guides, the differences in phenotype frequencies suggest that the location of the mutation influences phenotype penetrance.

Finally, we tested CRISPR-injected larvae for auditory and visual behaviors as before. In contrast to the stable chromodomain and ATP-helicase domain lines, all four injection conditions caused a reduction in SLC responses compared with Cas9-injected controls (Figure 5A,B). LLC responses were reduced only in larvae injected with all 3 gRNAs (Figure 5C,D). During the short-term habituation assay all injection conditions induced faster habituation of SLC responses (Figure 5E), and increased LLC responses during short-term habituation

TABLE 2 Morphological phenotype frequencies in crispants. Morphological phenotype ratio and frequencies in 5–6 dpf Cas9/*chd7* RNP-injected crispants.

	Craniofacial defect	Otolith defect	Pericardial edema	Noninflated swim bladder	Larvae with any morphological phenotype
Cas9 Control	-	-	-	-	0/73, 0.0%
Exon 3	-	3/32, 9.4%	5/32, 15.6%	2/32, 6.3%	11/32, 34.4%
Exon 9	2/32, 6.3%	6/32, 18.8%	2/32, 6.3%	8/32, 25%	15/32, 46.9%
Exon 30	3/40, 7.5%	8/40, 20%	7/40, 17.5%	7/40, 17.5%	15/40, 37.5%
Mix (3, 9, 30)	21/42, 50%	3/42, 7.1%	20/42, 47.6%	37/42, 88.1%	39/42, 92.9%

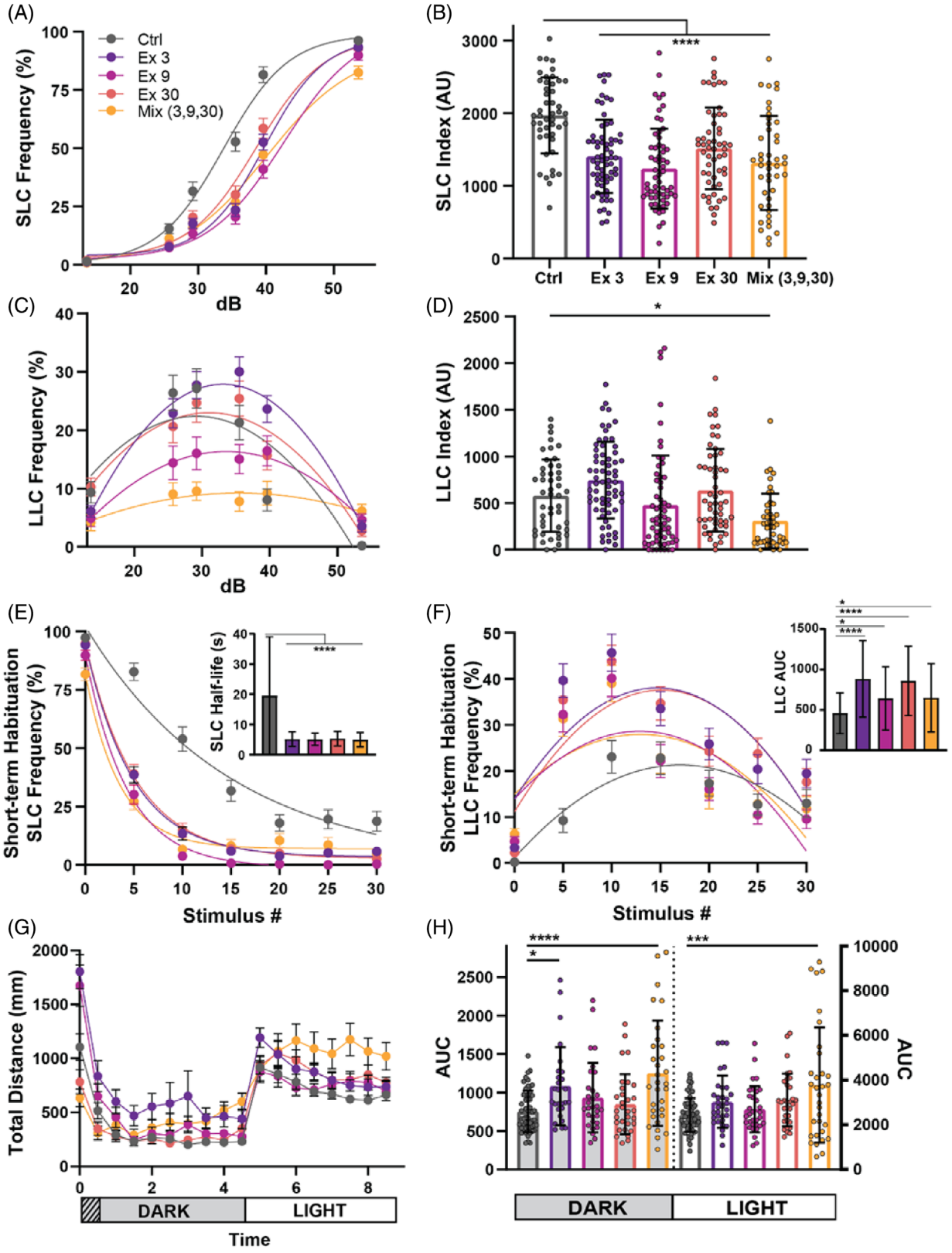

FIGURE 5 Legend on next page.

(Figure 5F), similar to our findings for both the stable chromodomain (Figure 2) and ATP-helicase domain alleles (Figure S4). In the long-term VMR assay, mixture-injected larvae displayed increased total distance traveled in both the dark and light phase compared with control injected siblings. Taken together, these results highlight that there are substantial phenotypic differences between CRISPR-injected

larvae and larvae derived from stable mutant lines. They also further illustrate that *chd7* loss of function in zebrafish produces CHARGE-related morphological and behavioral phenotypes, providing a powerful model system to understand the biological basis for these deficits.

4 | DISCUSSION

CHARGE syndrome is a heterogeneous condition with highly variable presentation that frequently includes many neurobehavioral features.[6,7,9,53,54] To better understand this heterogeneity, we generated multiple CHARGE models in zebrafish using CRISPR/Cas9 to target several locations within *CHD7*, the gene mutated in the majority of CHARGE cases.[12,15] Similar to the human disease, we observed variable penetrance of CHARGE-related morphological and behavioral phenotypes. Craniofacial, cardiac, visual, auditory, and locomotor defects, all of which are seen in CHARGE patients, were present in our larval zebrafish *chd7* mutants. These findings reinforce the validity of the zebrafish model for studying the pathogenesis of CHARGE syndrome, but more importantly our data provide new evidence that the location of mutations within the *CHD7* gene likely contributes to variation in the penetrance of CHARGE-related phenotypes.

Most mutations in *CHD7* leading to CHARGE syndrome are *de novo*, and they have been found throughout the gene as missense, nonsense, frameshift, splice site, and intronic mutations.[14–16] While there is no mutational hotspot that gives rise to the disease, whether the location of mutations may contribute to the variation in phenotypes present has not been clearly defined. We thus analyzed a set of patient data with well-defined phenotypes that included their corresponding *CHD7* mutation information.[16] Because this is a relatively small patient cohort and all mutation types (i.e., missense or nonsense) can be pathogenic, we grouped mutations together based on their domain location. All intronic mutations were grouped together regardless of location, and all of these cases were confirmed to be pathogenic splice variants. Through this analysis we found that patients with mutations in the histone-binding chromodomains presented with the highest percentage of all CHARGE phenotypes that were assessed, followed by those with mutations in the ATP helicase DEXDc domain, and the DNA-binding SANT domain (Figure 6).

This data is consistent with our findings in zebrafish larvae, in which chromodomain-targeted mutants (*chd7*$^{ncu101/}$) have higher rates of morphological phenotypes than larvae with mutations affecting the ATP-helicase domain (*chd7*$^{rdu1002/}$; Table 1). This includes highly penetrant otolith defects that were only observed in chromodomain mutants. Chromodomain mutants also show more behavioral deficits than ATP-helicase domain mutants (Table S2), having reduced Mauthner cell-independent long-latency startle responses (LLCs) following acoustic stimuli, reduced O-bend responses following dark-flash visual stimuli, and locomotor defects. ATP-helicase domain mutants did show hyperactivity while in the dark, a phenotype not seen in chromodomain mutants but one consistent with a recently described zebrafish *chd7* mutant with a different CRISPR-induced mutation in the ATP-helicase domain (Exon 17).[49] Our data also show that genetic background can contribute to variation in CHARGE-related phenotypes, as ATP-helicase domain mutants show reduced acoustic LLC responses when maintained in the TLF strain (Figure S6C,D), but not in the AB strain (Figure S4C,D). Similarly, we observed a higher rate of morphological phenotypes in chromodomain heterozygotes in the TLF strain (Table 1) than in those from a complementation cross to the AB-background ATP-helicase domain line (Table S1). Thus, the AB background may contain genetic modifiers that partially suppress some CHARGE-related phenotypes. Hyperactivity, however, was observed in ATP-helicase domain mutants independent of strain (Figure 4; Figures S7 and S8), but not in chromodomain mutants, highlighting the domain dependence of some behavioral phenotypes.

The domain-dependence of some CHARGE-related phenotypes also extended to our CRISPR-injected F_0 larvae ("crispants"). Those injected with CRISPR/Cas9 targeting the second chromodomain (Exon 9) had greater overall penetrance of developmental phenotypes such as craniofacial, otolith, and pericardial defects than those in which low complexity domains were targeted (Exon 3: low complexity 14; Exon 30: low complexity 24; Table 2). This pattern was not seen for the behavioral phenotypes we assessed, however, as larvae injected with a single gRNA had largely similar behavioral profiles regardless of the *chd7* target site. Larvae in which all three gRNAs were injected together showed the highest penetrance of both morphological and behavioral phenotypes, with 93% of injected larvae

FIGURE 5 CRISPR guides targeting different *chd7* Exons induce varying phenotypes. (A) Acoustic startle responses, average short-latency c-bend (SLC) frequency as acoustic stimulus intensity increases (Control $n = 47$, Exon 3 $n = 66$, Exon 9 $n = 60$, Exon 30 $n = 54$, Mix $n = 45$) (mean ± SEM). (B) Short-latency c-bend sensitivity index, calculated by the area under the SLC frequency curves for individual larvae (mean ± SD, Ordinary one-way ANOVA with Dunnett's multiple comparisons). (C) Long-latency c-bend (LLC) frequency as acoustic stimulus intensity increases (mean ± SEM). (D) Long-latency c-bend sensitivity index calculated by the area under the LLC frequency curves for individual larvae (mean ± SD, Ordinary one-way ANOVA with Dunnett's multiple comparisons). (E) Short-term habituation, average SLC frequency (Control $n = 48$, Exon 3 $n = 61$, Exon 9 $n = 59$, Exon 30 $n = 57$, Mix $n = 49$) (mean ± SEM) during 30 acoustic stimuli at highest intensity with (inset) SLC half-life calculated by nonlinear regression (one-phase exponential decay) of SLC frequency curves for individual larvae (mean ± SD, Ordinary one-way ANOVA with Dunnett's multiple comparisons). (F) Average LLC frequency (mean ± SEM) during 30 acoustic stimuli at highest intensity with (inset) LLC sensitivity index calculated by the area under the LLC frequency curves for individual larvae (mean ± SD, Ordinary one-way ANOVA with Dunnett's multiple comparisons). (G) Average total distance traveled plot during 9 h of recording, analyzed every 30 min, including 1 h of acclimation, 4 h in the dark, and 4 h in light (Control $n = 54$, Exon 3 $n = 27$, Exon 9 $n = 30$, Exon 30 $n = 31$, Mix $n = 31$) (mean ± SEM). (H) Area under the curve for individual larvae distance plots during the dark or light phase (mean ± SD, Ordinary one-way ANOVA with Dunnett's multiple comparisons, $^{*}p < 0.05$, $^{***}p < 0.001$,$^{****}p < 0.000$).

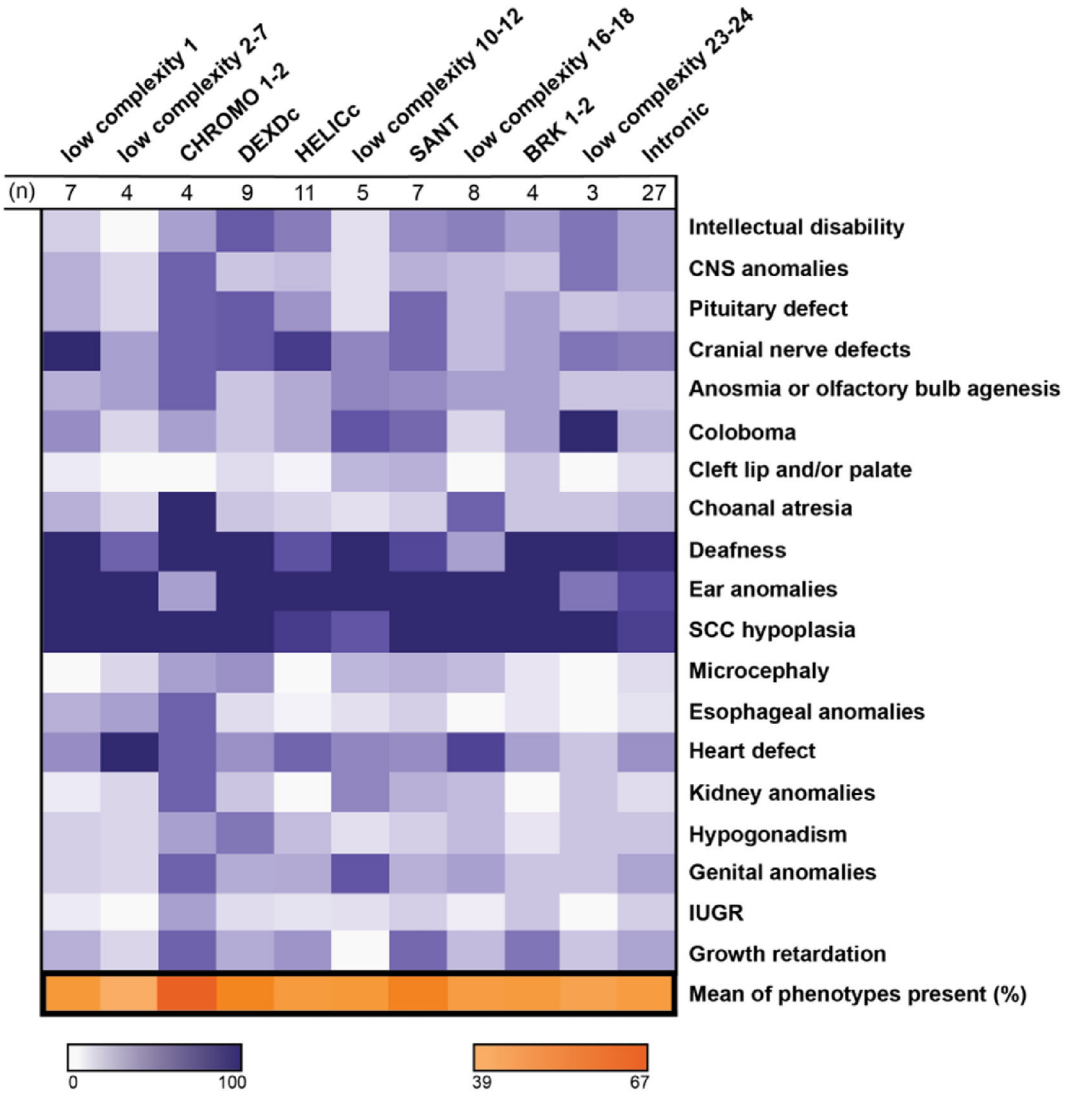

FIGURE 6 Correlation of mutation location and phenotype penetrance in a cohort of CHARGE patients. Heat map displaying the frequency of patients with a specified phenotype and a mutation within a particular *CHD7* domain; domains were determined by amino acid alignments ($n = 89$, $n = 30$ patients excluded from the original pool of 119 participants because of insufficient information or mutation did not align to a domain). CHD7 domains are represented by columns and phenotypes are represented by rows. Frequencies were calculated by the number of patients with a reported phenotype and mutation in the respective domain over the total number of patients within the same domain (purples). Final row represents the overall average phenotype frequency for a specific domain (oranges). Patient data was obtained from the paper *Phenotype and genotype analysis of a French cohort of 119 patients with CHARGE syndrome*, Legendre et al.[16] Darker colors indicate a higher frequency, with ranges indicated in the legends. CNS, central nervous system; IUGR, intrauterine growth restriction; SCC, semicircular canal.

having at least one morphological defect, along with significant defects in both Mauthner-dependent SLCs and Mauthner-independent LLCs and hyperactivity in both the dark and light phases of the visuo-motor response assay (Figure 5). The F_0 crispants differed in some respects from *chd7* mutants derived from our stable mutant lines, such as the SLC deficit that was not observed in stable mutants. As the same wild-type strain was used for all the F_0 crispants, these phenotypic differences are likely because of the mosaicism of the crispants or perhaps differences in genomic adaptation to the induced mutations between acutely injected larvae and those inheriting a single stable mutation. Because targeting early exons with CRISPR/Cas9 is a frequent strategy for attempting to create null alleles,[55] it is important to note that for *chd7* early-exon (Exon 3) crispants showed the fewest phenotypes even though a highly efficient guide was used (Figure S11). The presence of alternate *chd7* splice isoforms could also account for reduced phenotypes seen in the Exon 3 targeted larvae, but this is unlikely since the gRNA target site is present in all annotated transcripts. Our data show that *chd7* mutations not only produce variable phenotypes, but that the location of the targeted site, even if a premature stop codon is created, contributes to the expression of CHARGE-related phenotypes.

Our larval zebrafish CHARGE models recapitulate disease phenotypes seen previously in multiple animal systems, including *C. elegans*, *Drosophila*, *Xenopus*, zebrafish, and mouse. We have summarized

these CHARGE models' primary phenotypes in Table S3. In *C. elegans*, loss of *chd7* via RNA interference causes undetached cuticle, gonad migration defects, and stunted length.[56] Although we did not find significant differences in length and size in our zebrafish *chd7* mutants, mouse models have been reported to have delayed growth,[26] a symptom sometimes seen in CHARGE patients pre- and postnatally.[57–59] In *Drosophila*, mutations in *kismet*, the orthologue of *chd7*, cause movement deficits, eye defects, and wing abnormalities, as well as improper axon pruning, mislocalized neurons, and decreased glutamate receptor localization.[60,61] These defects in neural architecture in *kis*$^{-/-}$ may provide insight into potential mechanisms driving the deficits we see in our zebrafish model. However, *kismet* is an orthologue for both *chd7* and *chd8* in vertebrates and thus plays additional functional roles, including facilitation of transcriptional elongation.[62] Additionally, the reported alleles in *kis*$^{-/-}$ affect Exon 3, which contributes to most of the n-terminus of the protein including the chromodomains and ATP-helicase domain, making it difficult to compare phenotypes and potential domain dependence. *chd7* knock-down with a translation-blocking morpholino in *Xenopus* tadpoles resulted in similar morphological phenotypes to those in our zebrafish larvae, including craniofacial, heart, and otolith defects.[19] Finally, prior larval zebrafish CHARGE models have largely used morpholinos to knock down *chd7*, and these morphants display pericardial edema, craniofacial defects, and otolith defects,[28,30,37,40] similar to our chromodomain mutants. *Chd7* morphants also have neural crest cell migration defects,[28] reduced T-cell proliferation,[40] and disorganized retinal organization.[37] More recent CRISPR-generated *chd7* mutant larvae display similar morphological phenotypes to those in the present study including pericardial edema, craniofacial defects,[49] and uninflated swim bladders,[27] in addition to defects in gastrointestinal motility.[27] Together, these studies underscore the highly conserved and multiple roles of *chd7* in development.

In mice, homozygous *CHD7* mutations are embryonically lethal, so research has been largely limited to *CHD7*$^{+/-}$ derived from ENU mutagenesis.[26,51,63,64] *CHD7*$^{+/-}$ mice, like our zebrafish mutants, display ear and cardiovascular abnormalities (Table S3).[26] *CHD7*$^{+/-}$ also exhibit circling behaviors,[26] an indication of vestibular dysfunction, and reduced olfactory function.[22] Cerebellar-targeted *CHD7* conditional mutants show motor delays and coordination deficits.[21] We did not see evidence of vestibular or coordination deficits in our zebrafish models, and so these phenotypes could indicate unique roles for mammalian *CHD7*, but further analysis is needed as we did not examine limb movement in our locomotor assays because of the difficulty of imaging the movement of the pectoral fins in 5 dpf larvae. As with our zebrafish mutants and CHARGE patients, the CHARGE-related phenotypes in these mouse models are highly variable, including variation in the penetrance and severity of ear phenotypes between the multiple *CHD7* alleles with mutations in different parts of the gene.[26,51] Within one of these lines, *Whirligig*, phenotypes also had variable penetrance, with abnormalities in the ear and female external genitalia being highly penetrant (>90%), while eye, cardiovascular, palate, and olfactory defects having reduced penetrance (<50%),[14,22] despite using an inbred mouse strain. While zebrafish strains are fairly outbred and maintain significant genetic diversity,[65,66] our data also show variable penetrance of phenotypes within a single line. Furthermore, multiple sibling pairs with CHARGE syndrome that carry the same deleterious mutation in *CHD7* have been identified, with phenotypic differences between siblings.[15] Therefore, the *CHD7* mutation location and genetic background are not the only factors that give rise to phenotypic differences, and variation in the fetal microenvironment and developmental stochasticity also likely contribute to the heterogeneity of CHARGE phenotypes.[14]

The diverse roles of *CHD7* in the development of multiple tissues make for a challenge in determining the precise cellular and molecular pathways leading to each of the many CHARGE phenotypes. In the nervous system alone, *CHD7* promotes neuronal differentiation,[24,25,67,68] is required for proper neurite development,[69] regulates cerebellar organization through *RELN*,[21] promotes GABAergic neuron development through *paqr3*[49] and is required for neural crest cell differentiation and migration,[70,71] thereby contributing to multiple disease manifestations such as cranial nerve, cardiac, and craniofacial defects.[19] Our chromodomain mutants display both morphological defects in the ear and a deficit in auditory LLC responses (Figures 1 and 2). We found that the LLC deficit is independent of ear morphology, indicating that *chd7* likely regulates this behavior centrally (Figure 3). Defects in the auditory nerve could cause this phenotype, although the fact that SLC responses are normal following non-habituating acoustic stimuli suggests that the defect may be more specific to the LLC circuit, which includes a set of pre-pontine neurons in rhombomere 1.[41] During short-term habituation, however, SLC responses decrease faster and LLC responses are increased in *chd7* chromodomain mutants (Figure 2E–H), indicating that *chd7* also regulates the function of neurons that modulate these acoustic startle circuits. It is possible that abnormal GABAergic neuron development could underlie these defects,[49] as inhibitory input is crucial for normal habituation.[72]

In conclusion, our results provide additional support for the highly conserved roles of *CHD7* in the development of many tissues and processes, including the nervous system and behavior. Our findings underscore the highly heterogeneous nature of CHARGE phenotypes across model systems, but we also show new evidence that the location of mutations within *CHD7* contributes to variation in disease-related phenotypes. Finally, our new CHARGE models create opportunities for future efforts to take advantage of the larval zebrafish system to define brain-wide roles for *CHD7*, identify genetic modifiers of CHARGE-related phenotypes, and screen for compounds that may restore function in pre-clinical models of CHARGE.

AUTHOR CONTRIBUTIONS

Project conceptualization: Kurt C. Marsden and Dana R. Hodorovich. *Methodology*: Dana R. Hodorovich and Kurt C. Marsden. *Investigation*: Dana R. Hodorovich, Patrick M. Lindsley, Austen A. Berry, Derek F. Burton, and Kurt C. Marsden. *Data curation*: Dana R. Hodorovich, Patrick M. Lindsley, and Austen A. Berry. *Writing*: Dana R. Hodorovich, Patrick M. Lindsley, and Kurt C. Marsden; *Writing – review & editing*: Dana R. Hodorovich and Kurt C. Marsden; *Supervision*: Kurt C. Marsden; *Funding acquisition*: Kurt C. Marsden.

ACKNOWLEDGMENTS

We would like to thank Dr. Erica Davis (Northwestern University, Feinberg School of Medicine) for supplying the *chd7*$^{rdu1002/+}$ line. We are also grateful to Rachael Bieler for additional proofreading help with the manuscript.

FUNDING INFORMATION

This work was funded by the National Institute for Neurological Disease and Stroke (R21NS120079-01 to K.C.M.) and by a pilot grant from the CHARGE Syndrome Foundation to K.C.M.

CONFLICT OF INTEREST STATEMENT

The authors declare no competing or financial interests.

ORCID

Kurt C. Marsden https://orcid.org/0000-0001-8087-6181

REFERENCES

1. Zentner GE, Layman WS, Martin DM, Scacheri PC. Molecular and phenotypic aspects of CHD7 mutation in CHARGE syndrome. *Am J Med Genet A*. 2010;152A:674-686.
2. Verloes A. Updated diagnostic criteria for CHARGE syndrome: a proposal. *Am J Med Genet A*. 2005;133A:306-308.
3. Blake KD, Hartshorne TS, Lawand C, Dailor AN, Thelin JW. Cranial nerve manifestations in CHARGE syndrome. *Am J Med Genet A*. 2008;146A:585-592.
4. Blake KD, Prasad C. CHARGE syndrome. *Orphanet J Rare Dis*. 2006;1:34.
5. Blake KD, Salem-Hartshorne N, Daoud MA, Gradstein J. Adolescent and adult issues in CHARGE syndrome. *Clin Pediatr*. 2005;44:151-159.
6. Hartshorne TS, Stratton KK, Brown D, Madhavan-Brown S, Schmittel MC. Behavior in CHARGE syndrome. *Am J Med Genet C Semin Med Genet*. 2017;175:431-438.
7. Hartshorne TS, Grialou TL, Parker KR. Autistic-like behavior in CHARGE syndrome. *Am J Med Genet A*. 2005;133A:257-261.
8. Bernstein V, Denno LS. Repetitive behaviors in CHARGE syndrome: differential diagnosis and treatment options. *Am J Med Genet A*. 2005;133A:232-239.
9. Hartshorne N, Hudson A, MacCuspie J, et al. Quality of life in adolescents and adults with CHARGE syndrome. *Am J Med Genet A*. 2016;170:2012-2021.
10. Souriau J, Gimenes M, Blouin C, et al. CHARGE syndrome: developmental and behavioral data. *Am J Med Genet A*. 2005;133A:278-281.
11. Wachtel LE, Hartshorne TS, Dailor AN. Psychiatric diagnoses and psychotropic medications in CHARGE syndrome: a pediatric survey. *J Dev Phys Disabil*. 2007;19:471-483.
12. Vissers LELM, van Ravenswaaij CMA, Admiraal R, et al. Mutations in a new member of the chromodomain gene family cause CHARGE syndrome. *Nat Genet*. 2004;36:955-957.
13. Zentner GE, Hurd EA, Schnetz MP, et al. CHD7 functions in the nucleolus as a positive regulator of ribosomal RNA biogenesis. *Hum Mol Genet*. 2010;19:3491-3501.
14. Bergman JEH, Janssen N, Hoefsloot LH, Jongmans MCJ, Hofstra RMW, van Ravenswaaij-Arts CMA. CHD7 mutations and CHARGE syndrome: the clinical implications of an expanding phenotype. *J Med Genet*. 2011;48:334-342.
15. Jongmans MCJ, Admiraal RJ, van der Donk KP, et al. CHARGE syndrome: the phenotypic spectrum of mutations in the CHD7 gene. *J Med Genet*. 2006;43:306-314.
16. Legendre M, Abadie V, Attié-Bitach T, et al. Phenotype and genotype analysis of a French cohort of 119 patients with CHARGE syndrome. *Am J Med Genet C Semin Med Genet*. 2017;175:417-430.
17. Sanlaville D, Etchevers HC, Gonzales M, et al. Phenotypic spectrum of CHARGE syndrome in fetuses with CHD7 truncating mutations correlates with expression during human development. *J Med Genet*. 2006;43:211-217.
18. Schulz Y, Wehner P, Opitz L, et al. CHD7, the gene mutated in CHARGE syndrome, regulates genes involved in neural crest cell guidance. *Hum Genet*. 2014;133:997-1009.
19. Wysocka J, Chang C-P, Xiong Y, et al. CHD7 cooperates with PBAF to control multipotent neural crest formation. *Nature*. 2010;463:958-962.
20. Whittaker DE, Kasah S, Donovan APA, et al. Distinct cerebellar foliation anomalies in a CHD7 haploinsufficient mouse model of CHARGE syndrome. *Am J Med Genet C Semin Med Genet*. 2017;175C:465-477.
21. Whittaker DE, Riegman KLH, Kasah S, et al. The chromatin remodeling factor CHD7 controls cerebellar development by regulating reelin expression. *J Clin Invest*. 2017;127:874-887.
22. Bergman JEH, Bosman EA, van Ravenswaaij-Arts CMA, Steel KP. Study of smell and reproductive organs in a mouse model for CHARGE syndrome. *Eur J Hum Genet*. 2010;18:171-177.
23. Layman WS, McEwen DP, Beyer LA, et al. Defects in neural stem cell proliferation and olfaction in Chd7 deficient mice indicate a mechanism for hyposmia in human CHARGE syndrome. *Hum Mol Genet*. 2009;18:1909-1923.
24. He D, Marie C, Zhao C, et al. Chd7 cooperates with Sox10 and regulates the onset of CNS myelination and remyelination. *Nat Neurosci*. 2016;19:678-689.
25. Jones KM, Saric N, Russell JP, Andoniadou CL, Scambler PJ, Basson MA. CHD7 maintains neural stem cell quiescence and prevents premature stem cell depletion in the adult hippocampus. *Stem Cells*. 2015;33:196-210.
26. Bosman EA, Penn AC, Ambrose JC, Kettleborough R, Stemple DL, Steel KP. Multiple mutations in mouse Chd7 provide models for CHARGE syndrome. *Hum Mol Genet*. 2005;14:3463-3476.
27. Cloney K, Steele SL, Stoyek MR, et al. Etiology and functional validation of gastrointestinal motility dysfunction in a zebrafish model of CHARGE syndrome. *FEBS J*. 2018;285:2125-2140.
28. Asad Z, Pandey A, Babu A, et al. Rescue of neural crest-derived phenotypes in a zebrafish CHARGE model by Sox10 downregulation. *Hum Mol Genet*. 2016;25:3539-3554.
29. Asad Z, Sachidanandan C. Chemical screens in a zebrafish model of CHARGE syndrome identifies small molecules that ameliorate disease-like phenotypes in embryo. *Eur J Med Genet*. 2020;63:103661.
30. Balow SA, Pierce LX, Zentner GE, et al. Knockdown of fbxl10/kdm2bb rescues chd7 morphant phenotype in a zebrafish model of CHARGE syndrome. *Dev Biol*. 2013;382:57-69.
31. Burgess HA, Granato M. Sensorimotor gating in larval zebrafish. *J Neurosci*. 2007;27:4984-4994.
32. Burgess HA, Granato M. Modulation of locomotor activity in larval zebrafish during light adaptation. *J Exp Biol*. 2007;210:2526-2539.
33. Marsden KC, Jain RA, Wolman MA, et al. A Cyfip2-dependent excitatory interneuron pathway establishes the innate startle threshold. *Cell Rep*. 2018;23:878-887.
34. Howe K, Clark MD, Torroja CF, et al. The zebrafish reference genome sequence and its relationship to the human genome. *Nature*. 2013;496:498-503.
35. Friedrich RW, Jacobson GA, Zhu P. Circuit neuroscience in zebrafish. *Curr Biol*. 2010;20:R371-R381.
36. Kalueff AV, Stewart AM, Gerlai R. Zebrafish as an emerging model for studying complex brain disorders. *Trends Pharmacol Sci*. 2013;35:63-75.
37. Patten SA, Jacobs-McDaniels NL, Zaouter C, Drapeau P, Albertson RC, Moldovan F. Role of Chd7 in zebrafish: a model for CHARGE syndrome. *PLoS One*. 2012;7:e31650.
38. Nicolson T. The genetics of hearing and balance in zebrafish. *Annu Rev Genet*. 2005;39:9-22.

39. Schulz-Mirbach T, Ladich F, Plath M, Heß M. Enigmatic ear stones: what we know about the functional role and evolution of fish otoliths. *Biol Rev Camb Philos Soc*. 2019;94:457-482.
40. Liu ZZ, Wang ZL, Choi TI, et al. Chd7 is critical for early T-cell development and thymus organogenesis in zebrafish. *Am J Pathol*. 2018;188:1043-1058.
41. Marquart GD, Tabor KM, Bergeron SA, Briggman KL, Burgess HA. Prepontine non-giant neurons drive flexible escape behavior in zebrafish. *PLoS Biol*. 2019;17:e3000480.
42. Roberts AC, Reichl J, Song MY, et al. Habituation of the C-start response in larval zebrafish exhibits several distinct phases and sensitivity to NMDA receptor blockade. *PLoS One*. 2011;6:e29132.
43. Wolman MA, Jain RA, Liss L, Granato M. Chemical modulation of memory formation in larval zebrafish. *Proc Natl Acad Sci U S A*. 2011;108:15468-15473.
44. Jain RA, Wolman MA, Marsden KC, et al. A forward genetic screen in zebrafish identifies the G-protein-coupled receptor CaSR as a modulator of sensorimotor decision making. *Curr Biol*. 2018;28:1357-1369.e5.
45. Alexandre D, Ghysen A. Somatotopy of the lateral line projection in larval zebrafish. *Proc Natl Acad Sci U S A*. 1999;96:7558-7562.
46. Liao JC, Haehnel M. Physiology of afferent neurons in larval zebrafish provides a functional framework for lateral line somatotopy. *J Neurophysiol*. 2012;107:2615-2623.
47. Martin GC, Robert MP, Challe G, et al. Functional vision analysis in patients with CHARGE syndrome. *J Pediatr Ophthalmol Strabismus*. 2020;57:120-128.
48. Onesimo R, Ricci D, Agazzi C, et al. Visual function and ophthalmological findings in charge syndrome: revision of literature, definition of a new clinical spectrum and genotype phenotype correlation. *Genes*. 2021;12:972.
49. Jamadagni P, Breuer M, Schmeisser K, et al. Chromatin remodeller CHD7 is required for GABAergic neuron development by promoting PAQR3 expression. *EMBO Rep*. 2021;22:e50958.
50. Alavizadeh A, Kiernan AE, Nolan P, Lo C, Steel KP, Bucan M. The Wheels mutation in the mouse causes vascular, hindbrain, and inner ear defects. *Dev Biol*. 2001;234:244-260.
51. Kiernan AE, Erven A, Voegeling S, et al. ENU mutagenesis reveals a highly mutable locus on mouse Chromosome 4 that affects ear morphogenesis. *Mamm Genome*. 2002;13:142-148.
52. Pau H, Hawker K, Fuchs H, De Angelis MH, Steel KP. Characterization of a new mouse mutant, flouncer, with a balance defect and inner ear malformation. *Otol Neurotol*. 2004;25:707-713.
53. Hartshorne TS, Cypher AD. Challenging behavior in CHARGE syndrome. *Mental Health Asp Dev Disabil*. 2004;7:41-52.
54. Smith IM, Nichols SL, Issekutz K, Blake K, Canadian Paediatric Surveillance Program. Behavioral profiles and symptoms of autism in CHARGE syndrome: preliminary Canadian epidemiological data. *Am J Med Genet A*. 2005;133A:248-256.
55. Hoshijima K, Jurynec MJ, Klatt Shaw D, Jacobi AM, Behlke MA, Grunwald DJ. Highly efficient CRISPR-Cas9-based methods for generating deletion mutations and F0 embryos that lack gene function in zebrafish. *Dev Cell*. 2019;51:645-657.e4.
56. Jofré DM, Hoffman DK, Cervino AS, et al. The CHARGE syndrome ortholog CHD-7 regulates TGF-β pathways in Caenorhabditis elegans. *Proc Natl Acad Sci U S A*. 2022;119:e2109508119.
57. Antoniou M-C, Bouthors T, Xu C, et al. A novel CHD7 mutation in an adolescent presenting with growth and pubertal delay. *Ann Pediatr Endocrinol Metab*. 2019;24:49-54.
58. Kim JH, Choi Y, Hwang S, Kim G-H, Yoo H-W, Choi J-H. Phenotypic spectrum of patients with mutations in CHD7: clinical implications of endocrinological findings. *Endocr Connect*. 2022;11(2):e210522.
59. Traisrisilp K, Chankhunaphas W, Sittiwangkul R, Phokaew C, Shotelersuk V, Tongsong T. Prenatal sonographic features of CHARGE syndrome. *Diagnostics (Basel)*. 2021;11(3):415-424.
60. Ghosh R, Vegesna S, Safi R, et al. Kismet positively regulates glutamate receptor localization and synaptic transmission at the Drosophila neuromuscular junction. *PLoS One*. 2014;9:e113494.
61. Melicharek DJ, Ramirez LC, Singh S, Thompson R, Marenda DR. Kismet/CHD7 regulates axon morphology, memory and locomotion in a Drosophila model of CHARGE syndrome. *Hum Mol Genet*. 2010;19:4253-4264.
62. Srinivasan S, Armstrong JA, Deuring R, Dahlsveen IK, McNeill H, Tamkun JW. The Drosophila trithorax group protein Kismet facilitates an early step in transcriptional elongation by RNA polymerase II. *Development*. 2005;132:1623-1635.
63. Hrabé de Angelis MH, Flaswinkel H, Fuchs H, et al. Genome-wide, large-scale production of mutant mice by ENU mutagenesis. *Nat Genet*. 2000;25:444-447.
64. Nolan PM, Peters J, Strivens M, et al. A systematic, genome-wide, phenotype-driven mutagenesis programme for gene function studies in the mouse. *Nat Genet*. 2000;25:440-443.
65. Balik-Meisner M, Truong L, Scholl EH, Tanguay RL, Reif DM. Population genetic diversity in zebrafish lines. *Mamm Genome*. 2018;29:90-100.
66. Butler MG, Iben JR, Marsden KC, Epstein JA, Granato M, Weinstein BM. SNPfisher: tools for probing genetic variation in laboratory-reared zebrafish. *Development*. 2015;142:1542-1552.
67. Feng W, Kawauchi D, Körkel-Qu H, et al. Chd7 is indispensable for mammalian brain development through activation of a neuronal differentiation programme. *Nat Commun*. 2017;8:14758.
68. Feng W, Khan MA, Bellvis P, et al. The chromatin remodeler CHD7 regulates adult neurogenesis via activation of SoxC transcription factors. *Cell Stem Cell*. 2013;13:62-72.
69. Yao H, Hannum DF, Zhai Y, et al. CHD7 promotes neural progenitor differentiation in embryonic stem cells via altered chromatin accessibility and nascent gene expression. *Sci Rep*. 2020;10:1-15.
70. Fan X, Masamsetti VP, Sun JQ, et al. TWIST1 and chromatin regulatory proteins interact to guide neural crest cell differentiation. *Elife*. 2021;10:e62873.
71. Okuno H, Renault Mihara F, Ohta S, et al. CHARGE syndrome modeling using patient-iPSCs reveals defective migration of neural crest cells harboring CHD7 mutations. *Elife*. 2017;6:e21114.
72. Marsden KC, Granato M. In vivo Ca(2+) imaging reveals that decreased dendritic excitability drives startle habituation. *Cell Rep*. 2015;13:1733-1740.

SUPPORTING INFORMATION

Additional supporting information can be found online in the Supporting Information section at the end of this article.

How to cite this article: Hodorovich DR, Lindsley PM, Berry AA, Burton DF, Marsden KC. Morphological and sensorimotor phenotypes in a zebrafish CHARGE syndrome model are domain-dependent. *Genes, Brain and Behavior*. 2023;22(3):e12839. doi:10.1111/gbb.12839